

Sensing wave-front amplitude and phase with phase diversity

Stuart M. Jefferies, Michael Lloyd-Hart, E. Keith Hege, and James Georges

We show in benchtop experiments that wave-front phase estimation by phase diversity can be significantly improved by simultaneous amplitude estimation. Processing speed, which will be important for real-time wave-front control applications, can be enhanced by use of small-format detectors with pixels that do not fully sample the diffraction limit. Using an object-independent phase-diversity algorithm, we show that, for both pointlike and extended objects, the fidelity of the phase and amplitude estimates degrades gracefully, rather than catastrophically, as the sampling becomes coarser. We show in simulation that the same algorithm also improves the fidelity of image reconstruction of complex targets.

© 2002 Optical Society of America

OCIS codes: 010.1080, 100.3190, 100.5070, 120.5050.

1. Introduction

Phase diversity (PD) is an established technique used for determining the phase distortion in an incoming wave front. Since its introduction over 20 years ago,¹ PD has been used primarily to produce blur-free imagery by image postprocessing.^{2–5} It has also been used, to a lesser extent, to calibrate optical systems,⁶ most notably in the case of the figure error in the primary mirror of the Hubble Space Telescope.^{7–9}

PD can also be used as a wave-front sensor (WFS), an application in which it has practical advantages over standard techniques such as Shack–Hartmann sensing. Generally, the optical beam train for a PD sensor is simpler, and the spatial scales on which aberrations are sensed can be easily changed when the defocus in the PD system is adjusted. In addition, PD can be used with greatly extended sources. The algorithm is already well suited to slower applications, such as maintaining alignment of large non-rigid optical systems, both on the ground (e.g., the Gemini 8-m telescope¹⁰) and in space (e.g., the

planned Next Generation Space Telescope¹¹). Recent developments in the speed of computers and algorithms used to process PD data^{12,13} indicate that the potential may soon be realized for PD to provide a practical WFS for adaptive optics¹⁴ in the compensation of atmospheric aberration.^{12,13,15}

The PD method requires at least two images of the same source to be taken simultaneously through the aberrating medium with different (known) phase aberrations being added optically to each image. Recovery of the wave-front phase information from the recorded images is then normally achieved through nonlinear optimization of some metric that measures the difference between the recorded data and a model of the data obtained with a given wave-front estimate.

Numerical simulations suggest that the fidelity of the recovered phases from PD measurements should be high. However, in an experiment conducted through atmospheric turbulence, a comparison of the slopes of the wave-front phases, as obtained with PD, with those obtained directly with a Shack–Hartmann sensor viewing the same source showed a disappointingly low level of correlation.¹⁶ The authors of that study speculated that neglect in their model of variations in the wave-front amplitude was responsible.

For a point-source illuminator, the difficulty can be removed by direct measurement of the wave-front amplitudes at an image of the pupil. Furthermore, iterative phase-retrieval algorithms such as Gerchberg–Saxton that rely on the assumption that the illuminator is pointlike have been demonstrated

S. M. Jefferies (stuartj@ahpcc.unm.edu) is with the Maui Scientific Research Center, the University of New Mexico, 590 Lipoa Parkway, Kihei, Hawaii 96753. M. Lloyd-Hart (mhart@as.arizona.edu), E. K. Hege (hege@as.arizona.edu), and J. Georges (jgeorges@u.arizona.edu) are with the Center for Astronomical Adaptive Optics, University of Arizona, Tucson, Arizona 85721.

Received 17 May 2001; revised manuscript received 13 November 2001.

0003-6935/02/112095-08\$15.00/0

© 2002 Optical Society of America

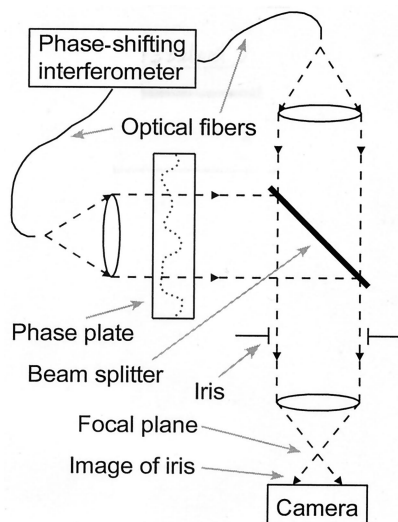


Fig. 1. Experimental setup used to record the true amplitude and phase variations, introduced by a plastic screen, and the phase-diverse focal-plane data.

to recover pupil illumination with complex structure with high accuracy.⁷⁻⁹

In the case of an extended source, a more general PD algorithm is required. Recovery of both wave-front amplitudes and phases has been demonstrated with simulated data,¹⁷ but real data inevitably have characteristics unknown to the experimenter, which are therefore not modeled in the simulations. Here we report the results of experiments with data from the optical bench in which we investigate the ability of PD to estimate the amplitude, as well as the phase, independently of the form of the illuminating object. We explore the effect of amplitude estimation on the fidelity of the recovered phase estimate.

A further consideration for use of PD as a WFS is the sampling of the focal-plane data. Typically the requirements for processing speed dictate use of small detector arrays, with images sampled as coarsely as possible without substantial loss of information. Chidlaw *et al.* have shown analytically¹⁸ that, for data sampled below the Nyquist limit, the solution for the wave front becomes nonunique. Here we investigate the practical effects of under-sampling the focal-plane data on the fidelity of the phase estimates.

Finally, we have begun to investigate the performance of the algorithm in the role of image reconstructor. We report results of object recovery for a slightly extended source in the benchtop experiments, and results of numerical simulations in which a more extended object with more complex structure is reconstructed.

2. Description of the Experiment

A. Experimental Setup

The experimental setup is shown in Fig. 1. Phase and amplitude aberrations were introduced by an acrylic plate, machined with thickness variations to

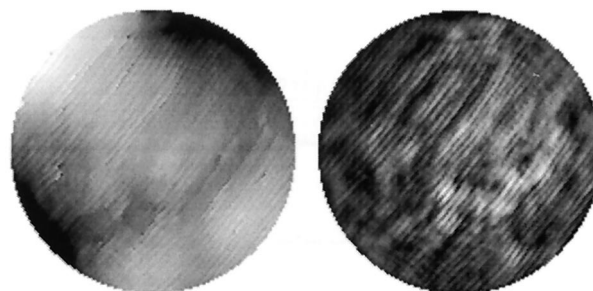


Fig. 2. Left, wave-front phases as measured by a phase-shifting interferometer. Right, the wave-front amplitudes (the square root of an intensity measurement in the pupil plane).

mimic the phase aberration expected in the free atmosphere. An iris placed downstream from the phase plate formed the imaging system's entrance pupil. We used three different configurations to record separately the phase, amplitude, and phase-diverse focal-plane image data, using a Pulnix camera digitized to 8 bits.

With the camera imaging the iris, a phase-shifting interferometer was used to measure the true phase aberration of light passing through a circular region on the plate. We recorded the amplitude variations across the same region by blocking the reference arm of the interferometer. The measured amplitudes and phases are shown in Fig. 2.

We then recorded a set of seven phase-diverse images of the unresolved laser illuminator by moving the camera back to positions equally spaced about the focal plane. In this configuration, the camera pixel size of $14\text{ }\mu\text{m}$ was closely matched to the diffraction-limited image width. A second set of phase-diverse images was recorded with an extended source provided by a roughly uniformly illuminated pinhole of $100\text{ }\mu\text{m}$ in diameter, subtending about seven diffraction widths at the detector. In each case, we removed the fixed-pattern detector effects by subtracting a dark frame recorded with the same integration time.

B. Characteristics of the Data

The overall tilt of the wave-front phase shown in Fig. 2 was subtracted because it affects only the image position. The root-mean-square (rms) deviation from a plane is 0.46λ at the laser's wavelength of $\lambda = 632.8\text{ nm}$. The amplitude (being the square root of the intensity recorded on the camera) has a rms variation of 0.412 , representative of strong scintillation. The high-frequency parallel lines running from the bottom left to the top right in the pictures in Fig. 2 are caused by the milling tool used to cut the acrylic plate.

Examples of the focal-plane image data are shown in Fig. 3. Each image is the first in a sequence of seven, taken at equally spaced intervals of 2.0λ peak-to-valley focus change along the optical axis. The top left panel shows the image of a point source recorded at the native pixel scale of the camera. To

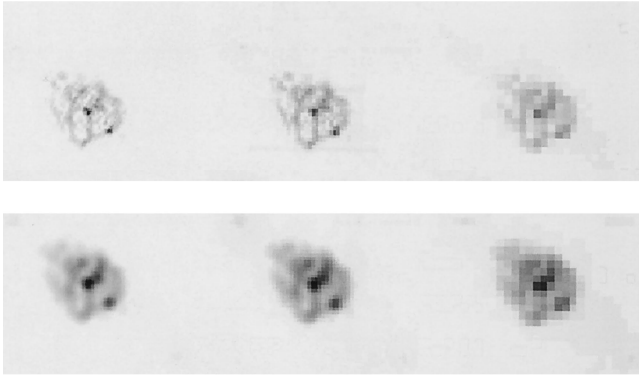


Fig. 3. Maximally defocused images for the six experiments conducted. Top row, images of a point source with, from left to right, no pixel binning, 2×2 , and 4×4 . Bottom row, corresponding images of an extended source.

investigate the effects of undersampling, each image in the sequence was binned 2×2 and 4×4 *post facto* in the computer. Similar sequences recorded and computed for the extended source are illustrated in the lower panels of Fig. 3. Faint secondary images can be seen at the top left and bottom right of each image, caused by the grating effect of the machine grooves in the phase plate.

When recording the image sequences, we adjusted the brightness of the source for each exposure so as to fill the camera's dynamic range. The appropriate photometric scaling was then taken into account in the PD algorithm to account correctly for the noise statistics of each individual data frame.

3. Estimation of the Complex Wave Front

A. Description of the Algorithm

We developed an iterative PD algorithm to estimate both the amplitude and the phase of the electric vector in the pupil simultaneously. As with a number of other algorithms, ours does not depend on the form of the illuminating object to derive its estimate of the complex wave front. We also account for undersampling in the data and the spatial correlations in the wave-front phases and amplitudes.

As with all PD algorithms, the general approach is to build a forward model of the imaging process by use of some estimate of the pupil-plane quantities. An error metric is computed from the differences between the modeled and the recorded images, and the wave-front estimates are refined iteratively to drive the metric to a minimum.

1. Initial Estimate of Low-Order Zernike Polynomial Coefficients

It is often the case in aberrated optical systems that phase distortions exhibit greater power at lower spatial frequencies. This is certainly true of aberrations caused by turbulence in the free atmosphere. Our algorithm therefore begins by estimating the coefficients of the lowest-order Zernike polynomials,

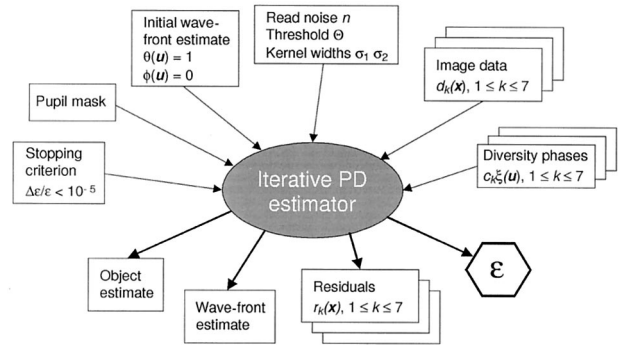


Fig. 4. Input-output scheme for the PD algorithm.

while assuming constant wave-front amplitudes. Figure 4 illustrates the algorithm schematically.

We assume initially that nothing is known about the complex wave front to be estimated except the window function defining the optical system's entrance pupil. Accordingly, the initial estimate of the wave front is set to unit amplitude within the pupil, zero outside it, and zero phase everywhere. The wave-front phase is modeled with

$$\psi(\mathbf{u}) = \sum_{j=4}^J q_j Z_j(\mathbf{u}), \quad (1)$$

where \mathbf{u} is a vector in the pupil plane and q_j is the coefficient of Zernike polynomial j . The first three Zernike polynomials (piston, tip, and tilt) are ignored. The PD algorithm estimates the coefficients q_j , and the value of J is increased gradually from 4 to 6 as the iteration progresses.

In principle, the wave-front amplitudes could also be estimated in this modal approach. The orthonormal properties of the Zernike basis set would allow it to be used for this purpose. The statistical properties of amplitude variations, however, at least those that arise from atmospheric scintillation that put more power at higher frequencies than is the case with phase aberrations, make low-order estimation less powerful.¹⁹ We therefore did not implement the approach in our code.

2. Construction of the Wave Front

After convergence of the algorithm on the Zernike coefficients, the wave-front amplitudes and high-order phase distortions are estimated at points on a square grid defined in the pupil. We begin by constructing a complex wave front from a pair of estimated functions $\theta(\mathbf{u})$ and $\phi(\mathbf{u})$. The pupil amplitude $P(\mathbf{u})$ is taken to be the square of the variable θ , to guarantee positivity, normalized to the unit volume:

$$P(\mathbf{u}) = \frac{N(\theta^2 \odot \eta_1)_{\mathbf{u}}}{[\sum_{\mathbf{u}'} W^2(\mathbf{u}') (\theta^2 \odot \eta_1)_{\mathbf{u}'}^2]^{1/2}}, \quad (2)$$

where N is the one-dimensional size of the data array, W is a circular window function, and \odot is the convolution operator. The pupil phase is given by

$$\psi(\mathbf{u}) = (\phi \odot \eta_2)_{\mathbf{u}}. \quad (3)$$

$$\eta_i(\mathbf{u}) = A_i \exp \left[- \left(\frac{u}{2\sigma_i} \right)^2 \right] \quad (4)$$

enforce the spatial correlation of the phases and amplitudes in Eqs. (2) and (3). The scalars A_i just normalize the kernels to unit volume, but the widths σ_i are used to prevent estimation of the wave-front structure on small spatial scales for which it is known *a priori* that no information is present in the data.

The main effect of the smoothing kernels is of course to reduce the high-spatial-frequency content in the estimates of the complex wave front. Frequencies that are poorly determined because of noise or focal-plane binning are thereby depreciated. A benefit of this approach is that the phase estimates are resistant to tears (jumps of 2π that are unphysical but have no effect on the focal-plane image).

Because the kernel values do not go to zero anywhere, smoothing of the wave front does not strictly forbid high spatial frequencies: No hard constraints are imposed on the power spectra of the estimated quantities θ and ϕ , thus allowing high frequencies that are well determined to grow. If the statistics of the wave-front perturbations are known in advance, then there are more rigorous ways to incorporate the prior knowledge about the phase and amplitude structures.^{20,21} However, there are many imaging situations in which the statistics are not known. In such cases, enforcing incorrect biases through use of an improper statistical model is likely to produce incorrect phase estimates. Our approach avoids the problem by suggesting correlation scales rather than forcing a spectral shape.

Because of the convolutions in Eqs. (2) and (3), values of P and ψ inside the telescope aperture are influenced by values outside. We therefore estimate θ and ϕ over a region that extends beyond the edges of W . The region is taken to be a band of width $2\sigma_i$ around W .

Introducing correlation has the further effect of reducing the number of nonequivalent (or independent) parameters to be determined. An unsmoothed circular window function of radius R pixels encompasses approximately πR^2 independent amplitude variables and the same number of phase variables. (The approximation arises because of the discrete nature of the pixels that do not exactly follow the circular border.) After we extend the region of estimation and perform smoothing, the number of independent parameters for each type of variable is $\sim (R + 2\sigma_i)^2 / \sigma_i^2$, which, for reasonable values of σ (i.e., $\sigma \geq 1$), is less than πR^2 .

3. Modeling the Point-Spread Function and Image Data

The incoherent point-spread function (PSF) $\hat{h}_k(\mathbf{x})$ is modeled in the familiar way as the squared modulus

of the Fourier transform of the optical system's pupil function:

$$\hat{h}_k = \hat{a}_k \hat{a}_k^*, \quad (5)$$

where $*$ represents the complex conjugate. By use of the amplitude model from Eq. (2) with the phase model from either Eq. (1) or Eq. (3), the coherent PSF is

$$\hat{a}_k(\mathbf{x}) = N^{-2} s_k \sum_{\mathbf{u}} W(\mathbf{u}) P(\mathbf{u}) \exp\{+i[\psi(\mathbf{u}) + c_k \xi(\mathbf{u})]\} \exp(-2\pi i u x / N). \quad (6)$$

Here \mathbf{x} is a vector in the image plane, subscript k indexes the diversity channel, and $\hat{}$ indicates an estimated quantity. Multiplication by s_k scales the model images to the same volume as the data, and ξ is the known diversity phase multiplied by known scalars c_k .

Both the Zernike coefficient and the point-by-point estimators represent the wave-front aberrations in the aperture of the imaging system. This near-field approximation allows us to compute image models $\hat{g}_k(\mathbf{x})$ as convolutions of an estimate of the object $\hat{f}(\mathbf{x})$ and the incoherent PSFs \hat{h}_k :

$$\hat{g}_k(\mathbf{x}) = \hat{f}(\mathbf{x}) \odot \hat{h}_k(\mathbf{x}). \quad (7)$$

The image data $d_k(\mathbf{x})$ recorded on the camera, however, may not in general adequately sample the diffraction limit, rendering Eq. (6) invalid. We can accommodate such undersampling by defining a new quantity $g_k(\mathbf{x})$ derived from the recorded data and correctly sampled to allow use of the Fourier transform to relate the pupil and focal planes:

$$g_k(\mathbf{x}) = d_k^\uparrow(\mathbf{x}) \odot b(\mathbf{x}). \quad (8)$$

Here \uparrow indicates an upsampling operator, that is, the replacement of each pixel in the original pixel grid by a block of $m \times m$ subpixels with the same value as the original. The block-replicated image is then smoothed through convolution with the boxcar function b , zero everywhere except for a square block of side m of unit value in the center.

4. Object Estimation

We derive the object estimate \hat{f} from a weighted cross spectrum of the data and the PSF estimates using the speckle holography equation²²:

$$\hat{f}(\mathbf{x}) = N^{-2} \sum_{\mathbf{u}} \left[\frac{\sum_k G_k(\mathbf{u}) \hat{H}_k^*(\mathbf{u})}{\gamma + \sum_k \hat{H}_k(\mathbf{u}) \hat{H}_k^*(\mathbf{u})} \right] \times \exp(-2\pi i u x / N), \quad (9)$$

where capital letters represent Fourier-transformed quantities. The regularizing parameter γ serves to prevent amplification of noise in $\sum_k G_k(\mathbf{u}) \hat{H}_k^*$ by low-amplitude spectral components of the PSF power spectrum estimate $\sum_k \hat{H}_k \hat{H}_k^*$. In practice we find that the intrinsic bias of the PSF spectrum is sufficiently nonzero to regularize the quotient, and the value of γ

is not critical. For the results of Section 4, γ was arbitrarily set to 10^{-5} .

5. Error Metric

Using the conjugate gradient optimization algorithm **fprmn** from *Numerical Recipes in C*,²³ we determine the best values for θ and ϕ by minimizing the autocorrelation function of the fitting residual. We use the error metric

$$\epsilon = \left\{ \sum_k \sum_{\mathbf{x} \neq 0} [r_k(\mathbf{x}) \star r_k(\mathbf{x})^2] \right\}^{1/2}, \quad (10)$$

where \star is the correlation operator. The residual

$$r_k(\mathbf{x}) = \frac{g_k(\mathbf{x}) - \hat{g}_k(\mathbf{x})}{[\hat{g}_k(\mathbf{x}) + n^2]^{1/2}} M_k(\mathbf{x}) \quad (11)$$

is the difference between the upsampled data and the modeled image, normalized by an estimate of the expectation value of the noise, and is masked by a binary function $M_k(\mathbf{x})$ expressing data support constraints.

The noise contamination of real data comprises both photon noise (Poisson statistics) and electronic read noise (Gaussian statistics). To accommodate this mixture of statistical distributions, while maintaining the relative simplicity of the Gaussian noise model for optimization purposes, we defined the noise variance in Eq. (11) as $\hat{g}_k(\mathbf{x}) + n^2$, where n is the measured rms read noise of the camera, taken to be the same at each pixel. The contribution from photon noise is estimated as \hat{g}_k and is allowed to vary at each iteration. At convergence, the residuals r_k approach a normal distribution with unit variance. A similar scheme has been used recently by Leung and Lane.²¹

The focal-plane mask $M_k(\mathbf{x})$ acts as a noise filter because it prevents inclusion of pixels with values smaller than a preset threshold Θ :

$$M_k(\mathbf{x}) = 1 \text{ for } g_k(\mathbf{x}) > \Theta \quad (12)$$

$$= 0 \text{ otherwise.} \quad (13)$$

In addition, M_k can be used to mask out bad pixels on the detector. The results presented in Section 4 were obtained with $\Theta = 2n$, twice the detector read noise.

We use Eq. (10) because of its intrinsic ability to enforce the prior knowledge that, for uncorrelated noise, any model that produces statistically correlated residuals is not the most likely model.²⁴ Our choice for ϵ measures the total power in the autocorrelation of the residual everywhere except at the origin. Because the autocorrelation of an uncorrelated function is a delta function at the origin, we expect the power everywhere else to be a minimum for uncorrelated residual errors.

B. Prescription for Wave-Front Estimation

The diversity phase introduced between the images in each sequence was modeled as a change in focus,

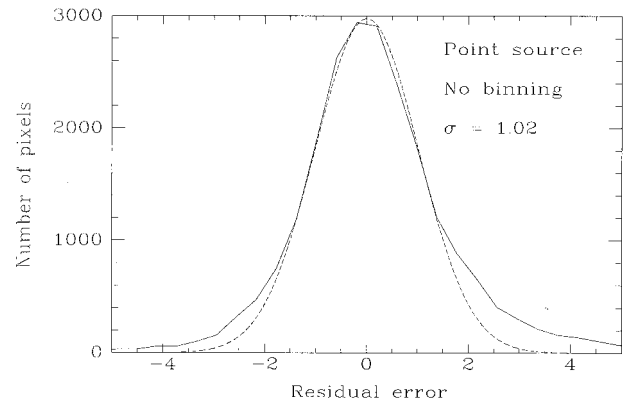


Fig. 5. Histogram of the residual focal-plane errors after convergence for the case of a point source with no binning. A Gaussian (dashed curve) was fitted to the core of the curve and has a standard deviation of 1.02, indicating that the wave front was estimated almost as closely as the noise in the image data will allow.

plus a tilt to accommodate a small misalignment between the system's mechanical and optical axes. We obtained an initial estimate of the phase error from the PD algorithm by assuming unit amplitude and estimating the three Zernike coefficients for the second-order aberrations focus and astigmatism. This phase estimate was then used as the starting point for a second round of computation in which the phases and amplitudes were estimated on a point-by-point basis.

Iteration of the PD algorithm was stopped when the error metric was changing by less than 1 part in 10^5 per iteration. Figure 5 illustrates the distribution of residuals in the focal plane after convergence for a typical case. Because the residuals are normalized by the expectation value of the noise in each pixel, they are expected to converge to a Gaussian distribution with unit standard deviation and zero mean. The distribution of Fig. 5 has wings that are somewhat too broad, but the core is well approximated by a Gaussian with a standard deviation of 1.02, indicating that the model was fitted to the data at a level consistent with the noise.

During the point-by-point estimation, Gaussian smoothing kernels were applied to the estimated quantities on each iteration. For the present data, information on scales smaller than a pixel is lost, so we chose the minimum width of the kernel to be commensurate with the degree of binning in each data set. We found that the algorithm converged more quickly, however, if the kernel widths were initially set to larger values. This had the effect of encouraging estimation first of the longer spatial scales that contained most of the power in the phase and amplitude aberration. Accordingly, the width σ_1 of the phase kernel was set initially to $0.1 \times$ the pupil diameter, corresponding to the spatial scale of the Zernike aberrations estimated in the first stage. Because no estimate of the amplitudes was made in the first stage, the amplitude kernel width σ_2 was set to $0.2 \times$ the pupil diameter. The algorithm was run

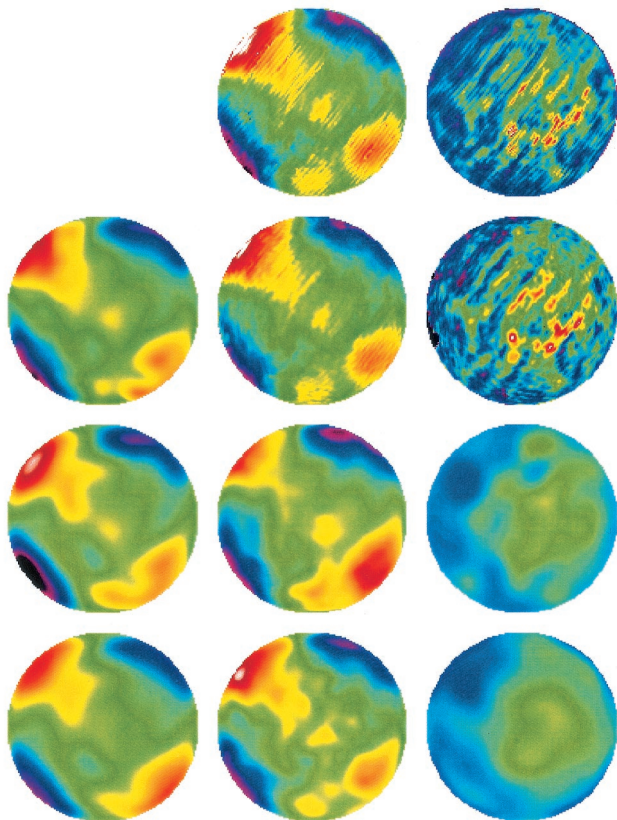


Fig. 6. Examples of reconstructed phases and amplitudes. Left column, phases reconstructed assuming unit amplitudes. Middle column, phases reconstructed with simultaneous amplitude estimation. Right column, estimated amplitudes. Top row, measured amplitudes and phases, repeated from Fig. 2. Second row, reconstruction from point-source data with no binning. Third row, point-source data with 4×4 binning. Bottom row, extended source data with 4×4 binning.

to convergence, at which point the kernel widths were reduced, and the process was repeated. For this study, the limits on σ_1 and σ_2 and the progressive reduction in size were done manually. There is no reason, however, why the process cannot be fully automated in a future upgrade to the algorithm.

4. Results and Discussion

A. Wave-Front Reconstruction

Examples of the reconstructions, including best and worst cases, are shown in Fig. 6. The measured amplitudes and phases are also shown for comparison. Table 1 shows residual rms phase and amplitude errors for the experiments in which both quantities were estimated. Table 2 lists the residual phase errors when the amplitudes were fixed at unity. In each case, allowing the amplitudes to vary improves the fidelity of the final phase estimate; the average improvement for the six cases here is 40%.

The results demonstrate, as expected, that the fidelity of the estimation suffers, particularly in the case of the amplitudes, as binning is increased. Nevertheless, in all cases in Table 1, the phase resid-

Table 1. Residual rms Phase and Amplitude Errors with Simultaneous Estimation

Source	Binning	Phase (rad)	Amplitude
Point	1	0.505	0.177
Point	2	0.580	0.235
Point	4	0.605	0.294
Extended	1	0.555	0.217
Extended	2	0.585	0.245
Extended	4	0.588	0.299

uals are well under 1 rad, allowing correction to Strehl ratios of ~ 0.75 in a wave-front compensation scheme. In contrast, the Strehl ratios achievable from the results of Table 2, without amplitude estimation, are ~ 0.5 . Furthermore, despite the severity of undersampling in the coarsest case (a factor of 8 compared with the Nyquist criterion), the degradation in the phase estimates is only approximately 20%. This can, at least in part, be attributed to the spatial statistics of the aberration, which closely follow the Kolmogorov spectrum expected in the atmosphere. When the images are binned, information is lost first on the smallest spatial scales, which are those scales containing the least power. This characteristic of the reduction in fidelity can be seen in the results of Fig. 6.

The degradation in the phase estimates with binning is less pronounced for the case of the extended source. This can perhaps be explained when we observe that, in this case, binning sacrifices less information. The effective resolution element of the imaging system is now no longer the diffraction limit, but the characteristic width of the object, in this case approximately seven times larger. After the convolution of the object with the PSF performed by the optics, and the addition of photon and digitization noise, the highest-spatial-frequency information is already lost. Binning, at least to the level where the pixel size matches the smallest features in the object, will not throw away significantly more information.

B. Object Reconstruction

Use of amplitude estimation is also of value when the aim of PD is to reconstruct the illuminating object rather than the wave front itself. This is illustrated in Fig. 7 that shows reconstructions of the pinhole source used in the benchtop experiments, with and

Table 2. Residual rms Phase Error without Simultaneous Amplitude Estimation

Source	Binning	Phase (rad)
Point	1	0.791
Point	2	0.807
Point	4	0.933
Extended	1	0.919
Extended	2	1.013
Extended	4	1.074

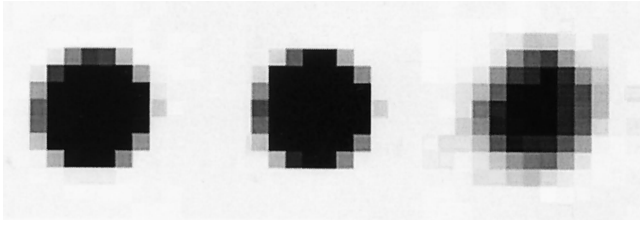


Fig. 7. Left, object estimate from unbinned image data with amplitude estimation. Center, true object image. Right, object estimate without amplitude estimation.

without amplitude estimation, and a direct image of the pinhole with the phase plate removed.

Amplitude estimation then can improve the reconstruction of an object as simple as a round pinhole. How well will the algorithm perform, however, when presented with a more complex object, and does amplitude estimation continue to be of value?

As a first step toward answering these questions, we simulated observations of a satellite in low Earth orbit. We made a set of PD images by convolving the blur-free target [Fig. 8(a)] with PSFs computed from the measured wave-front phase and amplitude distributions from the benchtop experiment. Seven diversity frames were computed, again with two waves of focus shift between them. The frame with zero defocus is shown in Fig. 8(b). Shot noise consistent with a total signal of 1×10^8 photons/frame and Gaussian noise simulating 10 electrons rms read noise were added. The flux is consistent with a 10-ms exposure of a low Earth orbit satellite directly overhead, imaged with a 3.5-m telescope. The same

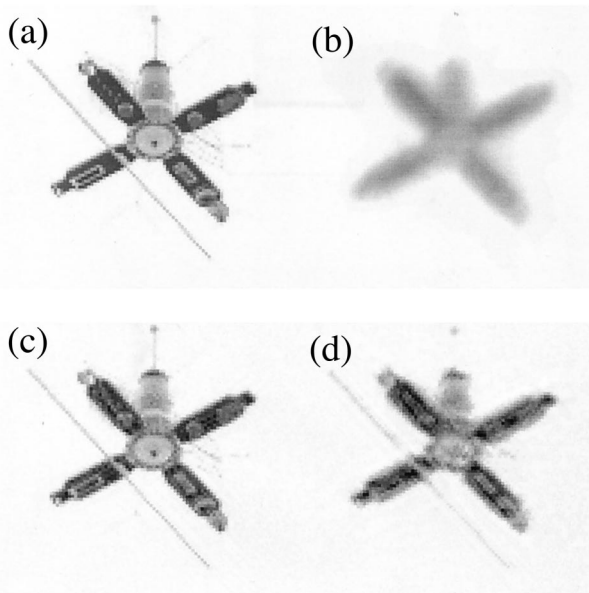


Fig. 8. (a) True object used for numerical simulation of object reconstruction. (b) Blurred image with photon and read noise added (best-focus frame from phase-diverse image set). (c) Reconstructed image with both phase and amplitude pupil-plane estimation. (d) Reconstructed image with phase-only estimation.

algorithm was applied, both with and without amplitude estimation.

The reconstructions, shown in Fig. 8(c) (with amplitude estimation) and Fig. 8(d) (without amplitude estimation), clearly show an improvement when amplitude estimation is used. By avoiding the pitfall of trying to force phase aberrations to account for effects in the data actually caused by amplitude variations, we can improve the estimate of the object's phase spectrum. This translates into a more faithful reconstruction of the unblurred object. Furthermore, the pupil-plane phases continue to be estimated more accurately when amplitudes are also estimated. In this case, the residual phase errors at convergence were 0.717- and 1.44-rad rms, with and without amplitude estimation, respectively.

These initial results are promising, suggesting that amplitude estimation can significantly improve the reconstruction of the target being imaged. Further research in this area is required, however, before a quantitative assessment can be made of the benefit to be expected for a general target of unknown morphology.

5. Conclusions and Future Directions

We have developed a PD algorithm that simultaneously estimates wave-front amplitudes and phases, as well as the form of the illuminating object. We have shown that the accuracy of phase estimation can be enhanced through simultaneous amplitude estimation, which is also likely to improve the fidelity of object reconstruction in the case of image restoration. The improvement is maintained even when the image is poorly sampled compared with the diffraction limit of the imaging system.

Wave-front sensing and image restoration problems generally incorporate a large number of parameters: signal level, detector noise, object size, shape, contrast ratio, background light level, and so on. Future research will explore the algorithm's performance in various regions of this parameter space in numerical simulation. In particular, we will examine the performance as a function of the number of diversity channels. In the research presented in this paper we have used seven channels for historical reasons relating to previous research on a time-of-flight approach to PD for wave-front sensing with pulsed laser beacons.¹⁵ We have no reason to believe, however, that this is in any sense an optimal number.

We will also explore the algorithm's expansion to include further information as constraints, in the sense that the forward model at convergence must reproduce the new data. For example, measurements of pupil-plane intensity, although they do not in general allow direct recovery of the wave-front amplitudes, can certainly be used in this way. In applications in which photon noise dominates, use of some of the light for pupil-plane measurements may give an advantage. In light-starved cases, however, a careful analysis would be required to determine the

effect on the signal-to-noise ratio before additional detectors were included.

With future advances in computer speed, the technique may become viable as a WFS with distinct advantages over current sensors. The reference beacon need not be unresolved or have any particular characteristic such as roundness, and the number of estimated degrees of freedom can be changed easily when the amount of defocus is varied in the phase-diverse channels.

This study has been supported by the U.S. Air Force Office of Scientific Research under grant F49620-99-1-0285 and the National Science Foundation under grant AST-9987358. We gratefully acknowledge the support of E. M. Hege and the University of Arizona Foundation.

References

1. R. A. Gonsalves and R. Chidlaw, "Wavefront sensing by phase retrieval," in *Applications of Digital Image Processing III*, A. G. Tescher, ed., Proc. SPIE **207**, 32–39 (1979).
2. R. G. Paxman, T. J. Schulz, and J. R. Fienup, "Joint estimation of object and aberrations by using phase diversity," J. Opt. Soc. Am. A **9**, 1072–1085 (1992).
3. M. G. Löfdahl and G. B. Scharmer, "Wavefront sensing and image restoration from focused and defocused solar images," Astron. Astrophys. **107**, 243–264 (1994).
4. J. H. Seldin, M. F. Reiley, R. G. Paxman, B. E. Stribling, B. L. Ellerbroek, and D. C. Johnston, "Space-object identification using phase-diverse speckle," in *Digital Image Recovery and Synthesis III*, T. J. Schulz, ed., Proc. SPIE **3170**, 2–15 (1997).
5. D. W. Tyler, S. D. Ford, B. R. Hunt, R. G. Paxman, M. C. Roggemann, J. C. Rountree, T. J. Schulz, K. J. Schulze, J. H. Seldin, D. G. Shepard, B. E. Stribling, W. C. van Kampen, and B. M. Welsh, "Comparison of image reconstruction algorithms using adaptive optics instrumentation," in *Adaptive Optical System Technologies*, D. Bonaccini and R. K. Tyson, eds., Proc. SPIE **3353**, 160–171 (1998).
6. R. G. Paxman and J. R. Fienup, "Optical misalignment sensing and image reconstruction using phase diversity," J. Opt. Soc. Am. A **5**, 914–923 (1988).
7. C. Roddier and F. Roddier, "Combined approach to the Hubble Space Telescope wave-front distortion analysis," Appl. Opt. **32**, 2992–3008 (1993).
8. J. R. Fienup, J. C. Marron, T. J. Schulz, and J. H. Seldin, "Hubble Space Telescope characterized by using phase-retrieval algorithms," Appl. Opt. **32**, 1747–1767 (1993).
9. J. E. Krist and C. J. Burrows, "Phase-retrieval analysis of pre- and post-repair Hubble Space Telescope images," Appl. Opt. **34**, 4951–4964 (1995).
10. M. Mountain, F. Gillett, and R. Kurz, "The Gemini 8m telescopes project," in *Optical Telescopes of Today and Tomorrow*, A. L. Ardeberg, ed., Proc. SPIE **2871**, 15–23 (1996).
11. For information on the Next Generation Space Telescope, see <http://www.ngst.nasa.gov>.
12. G. B. Scharmer, "Object-independent fast phase-diversity," in *High Resolution Solar Physics: Theory, Observations and Techniques*, T. Rimmele, R. R. Radick, and K. S. Balasubramaniam, eds., Astron. Soc. Pac. Conf. Ser. **183**, 330–341 (1999).
13. M. G. Löfdahl, G. B. Scharmer, and W. Wei, "Calibration of a deformable mirror and Strehl ratio measurements by use of phase diversity," Appl. Opt. **39**, 94–103 (2000).
14. R. A. Gonsalves, "Phase retrieval and diversity in adaptive optics," Opt. Eng. **21**, 829–832 (1982).
15. M. Lloyd-Hart, S. M. Jefferies, E. K. Hege, and J. R. P. Angel, "Wave-front sensing with time-of-flight phase diversity," Opt. Lett. **26**, 402–404 (2001).
16. J. H. Seldin, B. J. Thelan, D. A. Carrara, R. G. Paxman, J. J. Miller, and W. B. van Kampen, "Phase-diverse wavefront sensing and multi-frame image reconstruction," ERIM International Rep. 463000-7-F (Environmental Research Institute of Michigan, Ann Arbor, Mich., 1999).
17. R. A. Gonsalves, "Compensation of scintillation with a phase-only adaptive optic," Opt. Lett. **22**, 588–590 (1997).
18. R. Chidlaw, A. Devaney, and R. A. Gonsalves, "Analytical studies of phase estimation techniques," Defense Technical Report RADC-TR-79-221-Vol. 1 (Rome Air Development Center, Griffiss Air Force Base, New York, 1979).
19. D. Dravins, L. Lindegren, E. Mezey, and A. Young, "Atmospheric intensity scintillation of stars. I. Statistical distributions and temporal properties," Publ. Astron. Soc. Pac. **109**, 173–207 (1997).
20. R. Irwan and R. G. Lane, "Phase retrieval with prior information," J. Opt. Soc. Am. A **15**, 2302–2311 (1998).
21. W.-Y. V. Leung and R. G. Lane, "Blind deconvolution of images blurred by atmospheric speckle," in *Image Reconstruction from Incomplete Data*, M. A. Fiddy and R. P. Millane, eds., Proc. SPIE **4123**, 73–83 (2000).
22. E. K. Hege, "First order imaging methods: an introduction," in *Diffraction-Limited Imaging with Very Large Telescopes*, D. M. Alloin and J.-M. Mariotti, eds. (Kluwer Academic, Boston, Mass., 1989), pp. 113–124.
23. W. H. Press, S. A. Teukolsky, W. T. Vetterling, and B. P. Flannery, *Numerical Recipes in C*, 2nd ed. (Cambridge, U. Press, Cambridge, UK, 1992).
24. R. K. Piña and R. C. Puetter, "Incorporation of spatial information in Bayesian image reconstruction: the maximum residual likelihood criterion," Publ. Astron. Soc. Pac. **104**, 1096–1103 (1992).